Ocean Sci., 10, 907–921, 2014
www.ocean-sci.net/10/907/2014/
doi:10.5194/os-10-907-2014

Ocean Science
Open Access

On the glacial and interglacial thermohaline circulation and the associated transports of heat and freshwater

M. Ballarotta[1], S. Falahat[2], L. Brodeau[2], and K. Döös[2]

[1]Department of Physical Geography and Quaternary Geology, Bolin Centre for Climate Research, Stockholm University, 106 91 Stockholm, Sweden
[2]Department of Meteorology/Oceanography, Bolin Centre for Climate Research, Stockholm University, 106 91 Stockholm, Sweden

Correspondence to: M. Ballarotta (maxime.ballarotta@natgeo.su.se)

Received: 20 February 2014 – Published in Ocean Sci. Discuss.: 20 March 2014
Revised: 2 October 2014 – Accepted: 17 October 2014 – Published: 19 November 2014

Abstract. The thermohaline circulation (THC) and the oceanic heat and freshwater transports are essential for understanding the global climate system. Streamfunctions are widely used in oceanography to represent the THC and estimate the transport of heat and freshwater. In the present study, the regional and global changes of the THC, the transports of heat and freshwater and the timescale of the circulation between the Last Glacial Maximum (LGM, $\approx$ 21 kyr ago) and the present-day climate are explored using an Ocean General Circulation Model and streamfunctions projected in various coordinate systems. We found that the LGM tropical circulation is about 10 % stronger than under modern conditions due to stronger wind stress. Consequently, the maximum tropical transport of heat is about 20 % larger during the LGM. In the North Atlantic basin, the large sea-ice extent during the LGM constrains the Gulf Stream to propagate in a more zonal direction, reducing the transport of heat towards high latitudes by almost 50 % and reorganising the freshwater transport. The strength of the Atlantic Meridional Overturning Circulation depends strongly on the coordinate system. It varies between 9 and 16 Sv during the LGM, and between 12 to 19 Sv for the present day. Similar to paleo-proxy reconstructions, a large intrusion of saline Antarctic Bottom Water takes place into the Northern Hemisphere basins and squeezes most of the Conveyor Belt circulation into a shallower part of the ocean. These different haline regimes between the glacial and interglacial period are illustrated by the streamfunctions in latitude–salinity coordinates and thermohaline coordinates. From these diagnostics, we found that the LGM Conveyor Belt circulation is driven by an enhanced salinity contrast between the Atlantic and the Pacific basin. The LGM abyssal circulation lifts and makes the Conveyor Belt cell deviate from the abyssal region, resulting in a ventilated upper layer above a deep stagnant layer, and an Atlantic circulation more isolated from the Pacific. An estimate of the timescale of the circulation reveals a sluggish abyssal circulation during the LGM, and a Conveyor Belt circulation that is more vigorous due to the combination of a stronger wind stress and a shortened circulation route.

1 Introduction

The thermohaline circulation (THC) is the large-scale ocean circulation associated with the transports of heat and salt (Wunsch, 2002). The THC is known to play an important role for the climate variability (Knight et al., 2005; Zhang et al., 2007). In the North Atlantic region, it is characterised by an overturning circulation, the Atlantic Meridional Overturning Circulation (AMOC), which is often used as an indicator for climate change (Letcher, 2009). In the present-day climate, this AMOC contributes to a large amount of the heat transport (about 1.3 PetaWatt) from the tropics to higher latitudes (Ganachaud and Wunsch, 2000). It also plays an important role in the oceanic uptake of CO_2 (Zickfeld et al., 2008), the ventilation of the deep ocean (Keigwin and Schlegel, 2002; Bryan et al., 2006) and the reorganisation of passive and active tracers (e.g. temperature, salinity, greenhouse gases, nutrients). Several studies suggest that the intensity of the AMOC may have been different during glacial

climate and might also change in a near future under increased greenhouse gas forcing (see e.g. Manabe and Stouffer, 1994; Rahmstorf, 2002; Schmittner et al., 2005).

Our understanding of the past THC relies on reconstructions based on paleo-proxies and climate model experiments. The reconstructions of the Last Glacial Maximum (LGM, $\approx$21 kyr ago) ocean circulation using paleo-proxy records suggest that the AMOC was shallower due to a large intrusion of the Antarctic Bottom Water (AABW) in the North Atlantic (Curry, 2005; Marchitto and Broecker, 2006; Evans and Hall, 2008; Lippold et al., 2012). In various numerical experiments the AMOC responds differently to the LGM forcing and most models do not capture the geometry of the THC derived from the paleo-proxies (Otto-Bliesner et al., 2007; Weber et al., 2007). It is also important to point out that the integration of the climate models is often not long enough to draw firm conclusions on the abyssal THC. Therefore, most studies of the LGM THC focus on the North Atlantic, but the Southern Ocean also participates in the formation of the abyssal water, and the oceanic uptake of heat and carbon dioxide from the atmosphere (Gruber et al., 2009).

Streamfunctions are widely used to investigate and represent the ocean circulation. They show the averaged circulation in a two-dimensional framework and capture the wind-driven and the thermohaline contributions. The latitude–depth coordinates (see e.g. Fig. 2a) characterise the most common framework to diagnose the THC. In this coordinate system, the THC is represented by two near-surface tropical cells, an intermediate cell, the AMOC, representative of the North Atlantic Deep Water (NADW) between 40° S and 80° N; a Southern Ocean cell between 40 and 60° S (known as the Deacon Cell), and a deep-ocean circulation related to the AABW. However, the transport within the cells can strongly depend on the choice of coordinate system, especially when one considers the Southern Ocean circulation. Several studies point out that the Southern Ocean Cell in latitude–depth coordinates does not represent the observed Southern Ocean overturning circulation, which must be evaluated in latitude–density coordinates (McDougall, 1987; Döös and Webb, 1994; Hirst et al., 1996; Lee and Coward, 2003) or streamline coordinates (Treguier et al., 2008; Viebahn and Eden, 2012). Similarly, a better estimate of the present-day AMOC is obtained in latitude–density coordinates than in latitude–depth coordinates by Zhang et al. (2007) and Grist et al. (2012). This reinforces the necessity of investigating the THC in latitude–density coordinates rather than in latitude–depth coordinates.

The ocean meridional heat and freshwater transports are important for understanding the global climate system in terms of energy and water budgets (e.g. sea level change, ocean hydrological cycle). The meridional heat transport of the different overturning cells can be evaluated using the overturning streamfunction calculated in latitude–temperature coordinates (Ferrari and Ferreira, 2011). Similarly, the freshwater transport can evaluated from an overturning streamfunction calculated in latitude–salinity coordinates (see e.g. the *Baltic haline conveyor belt* in Döös et al., 2004; Blanke et al., 2006). Recently, Döös et al. (2012) and Zika et al. (2012) have presented a novel representation of the present-day THC by introducing a thermohaline streamfunction, i.e. the volume transport in salinity–temperature coordinates. It also allows estimation of the transport of heat and freshwater as well as the turnover time of the Conveyor Belt circulation (Broecker, 1991).

In the present study, we investigate the regional and global change of the THC between the LGM and the present day from a numerical experiment. We use a combination of streamfunctions computed in various coordinate systems to examine the thermohaline transformation, the transport of heat and freshwater and the timescale of the circulation between the glacial and interglacial period. The ocean model is integrated long enough to investigate the deep ocean circulation. After introducing the experimental design in Sect. 2, the streamfunctions in geographical coordinates and the thermohaline streamfunction are presented and discussed with regard to other climate simulations and proxy-reconstructions.

2 Methods

Streamfunctions were computed from the three-dimensional temperature, salinity and velocity fields originating from integrations carried out with the ocean general circulation model NEMO (Madec, 2008). NEMO is the ocean component of several coupled Earth-system models (Hazeleger et al., 2010; Voldoire et al., 2012; Dufresne et al., 2013) and is used extensively to perform hindcast (Barnier et al., 2007) and forecast (Storkey et al., 2010) simulations. It solves the primitive equations and in our experiments was integrated with a $1° \times 1°$ grid resolution, namely ORCA1. It had 64 vertical levels with a refined mesh near the surface and adaptive bottom boxes (partial-step method) for a better representation of the bathymetry (Barnier et al., 2006). Temperature and salinity were linked to the density via the nonlinear equation of state (Jackett and McDougall, 2003). The sub-grid parameterization of horizontal turbulent processes was based on the Gent and McWilliams (1990) formulation and hence an eddy-induced velocity was taken into account in the computation of the streamfunctions. The ocean model was coupled every 2 model-hours with the multilayer thermodynamic-dynamic LIM sea-ice model version 2 (Fichefet and Morales Maqueda, 1997). LIM computes the thermodynamic growth and decay of the sea-ice, as well as its dynamics and transport and takes into account the subgrid-scale effects of snow and ice thickness.

The two following experiments were designed:

1. A present-day ocean-only hindcast simulation forced by an ERA40-based atmospheric forcing covering 1958 to 2006 (Brodeau et al., 2010). This experiment is referred to as "PD_E".

2. A LGM ocean-only simulation forced by a 49 yr long atmospheric forcing and an initial state extracted from a coupled experiment by Brandefelt and Otto-Bliesner (2009). This experiment, referred to as "LGM_E", is also described by Ballarotta et al. (2013a, b).

A comparison between the ERA-40 and the LGM atmospheric forcing is provided in the Supplement (Fig. S1) as well as in Ballarotta et al. (2013b). In the tropical band, it is about 3 °C colder and 7 g kg^{-1} drier in LGM_E compared to PD_E. The maximum zonal and meridional 10 m wind velocities are about 1 m s^{-1} stronger. Due to reduced cloud cover and lower greenhouse-gas concentrations, the short-wave radiation is about 8 W m^2 larger and the long-wave radiation is about 20 W m^2 smaller in LGM_E than in PD_E. The mid-latitude region receives a larger amount of snow precipitation in LGM_E than in PD_E, but the zonally averaged total precipitation is smaller. The maximum zonal and meridional 10 m wind velocities are larger and slightly shifted equatorward in LGM_E than in PD_E. It is about 2 g kg^{-1} drier in LGM_E than PD_E. The short-wave radiation is similar whereas the long-wave radiation is about 20 W m^{-2} smaller in LGM_E than in PD_E. In the polar region, it is about 20 °C colder and drier (reduced precipitation) in LGM_E than in PD_E. The short-wave radiation is about 20 W m^{-2} larger in LGM_E and the long-wave radiation is 50 W m^{-2} smaller. The zonal and meridional winds over the ocean surface are stronger in LGM_E.

NEMO was run for a period of 1000 years by periodically repeating the surface atmospheric forcing. Our analysis is based on the last 50 years of each experiment. The simulations have a weak drift after 1000 years (see Fig. S2, in the Supplement). The globally averaged temperature trends in the upper 1000 m were less than 0.05 °C Century^{-1} in LGM_E and less than 0.2 °C Century^{-1} in PD_E. The temperature trends in the deep ocean (below 1000 m) were less than 0.02 °C Century^{-1} in both runs. The globally averaged salinity trends were weak (less than 0.02 PSU Century^{-1}).

3 Results and discussion

In this section, the THCs in LGM_E and PD_E are analysed using streamfunctions projected in various coordinate frameworks. The maxima of the overturning cells are summarised in Table 1.

3.1 Transports in geographical coordinates

3.1.1 Barotropic streamfunction and streamfunction in latitude–depth coordinates

The barotropic streamfunction gives the vertically averaged circulation in longitude–latitude coordinates. In this coordinate system, the circulation consists of basin-scale gyres (Fig. 1). The volume transport is more vigorous in LGM_E than in PD_E due to the larger wind stress acting on the ocean surface during the glacial period (see the zonally averaged zonal and meridional wind stress over the ocean in the right panels of Fig. 1). In LGM_E, the maxima of the volume transport in the North Atlantic and the North Pacific subtropical gyres are 30 and 50 Sv, respectively. They are about 20 Sv stronger than in PD_E. The zonal component of the Gulf Stream Extension is larger in LGM_E and the sea-ice extent is larger and reaches about 40° N. The maximum of the volume transport in the Atlantic and the Indian Ocean tropical gyres are rather similar (10 Sv) for the two experiments. In the Pacific basin, the circulations related to the tropical gyres are about 20 Sv stronger in LGM_E than in PD_E. The volume transport associated with the Agulhas leakage from the Indian Ocean to the South Atlantic basin seems to be less important in LGM_E, suggesting that the exchange of water properties from the Indian Ocean to South Atlantic basins is weaker in LGM_E than in PD_E. However, the mechanism of the Agulhas leakage is poorly resolved in coarse-resolution ocean models, and the realistic transport between the Indian and the South Atlantic basins might not be well represented. In the Southern Ocean, the volume transport is large due to the strong winds. In each experiment, the strength of the Antarctic Circumpolar Current (ACC) transport is about 130 Sv.

The THC is commonly investigated in the latitude–depth coordinates. In this coordinate system (see Fig. 2), the THC is represented by: (1) two near-surface inter-tropical cells;

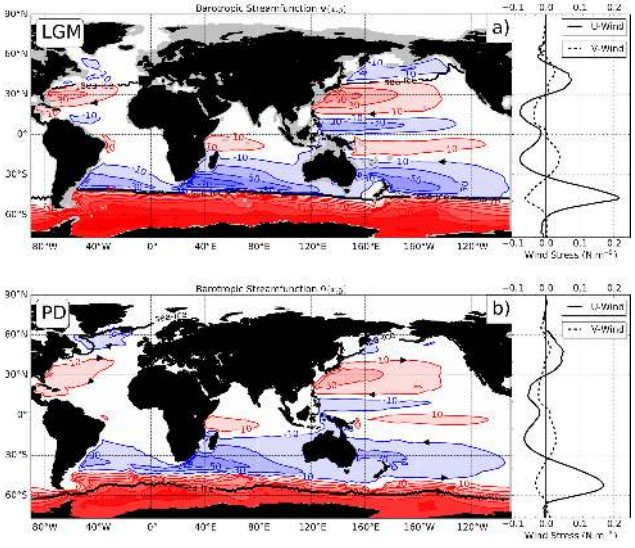

Figure 1. Barotropic streamfunctions for **(a)** the LGM simulation and **(b)** the PD simulation. The contour interval for the circulation is 20 Sv. Red contours indicate clockwise circulations and blue contours are for anti-clockwise circulations. The thick black line corresponds to the maximum sea-ice extent. Left diagram shows the time and zonally averaged zonal wind stress (U Wind) and meridional wind stress (V Wind) over the ocean

Table 1. Maximum volume transport in the LGM_E and PD_E simulations in the tropical cells, the AMOC cell, the Deacon Cell, the deep cell representative of the AABW (in the Atlantic basin and the global ocean) and the Conveyor Belt cell for the different coordinates frameworks.

	$\Psi(y,z)^{max}$		$\Psi(y,\gamma)^{max}$		$\Psi(y,\theta)^{max}$		$\Psi(y,S)^{max}$		$\Psi(S,\theta)^{max}$	
	LGM_E	PD_E	LGM_E	PD_E	LGM_E	PD_E	LGM_E	PD_E	LGM_E	PD_E
Tropical cell	≈ 35 Sv	≈ 35 Sv	≈ 30 Sv	≈ 27 Sv	≈ 30 Sv	≈ 26 Sv	≈ 20 Sv	≈ 20 Sv	24 Sv	21 Sv
AMOC	13 Sv	13 Sv	9 Sv	13 Sv	16 Sv	19 Sv	10 Sv	12 Sv		
Deacon cell/Residual cell	28 Sv	24 Sv	13 Sv	13 Sv	4 Sv	8 Sv	29 Sv	30 Sv		
Deep cell	19 Sv	8 Sv	12 Sv	16 Sv	41 Sv	44 Sv	10 Sv	18 Sv		
Deep cell (in Atlantic basin)	2 Sv	2 Sv	2 Sv	2 Sv	2 Sv	4 Sv	17 Sv	6 Sv		
Conveyor Belt cell									20 Sv	23 Sv

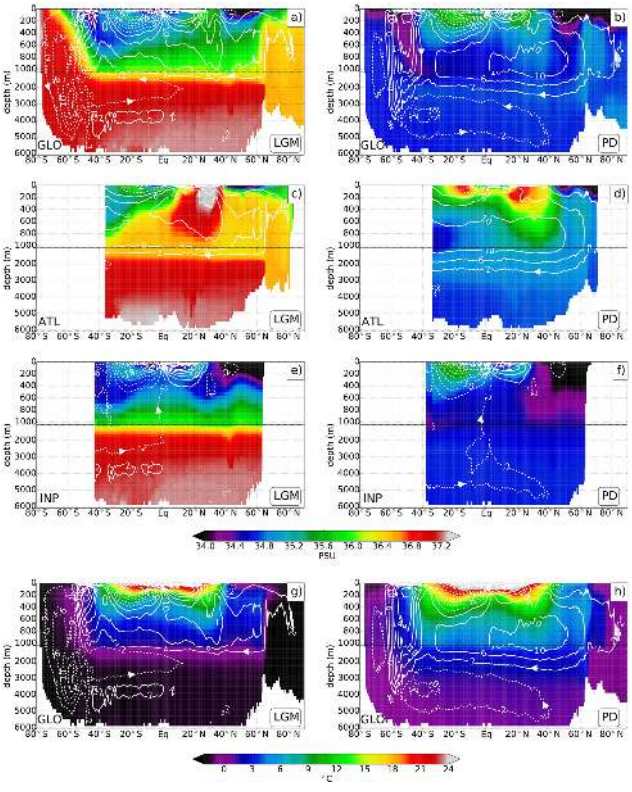

Figure 2. LGM and PD meridional overturning circulation in latitude–depth coordinates superimposed on the temporally and zonally averaged salinity in the Global Ocean **(a, b)**, the Atlantic basin **(c, b)** and the Indo-Pacific basin **(e, f)**. In the lower panels **(g)** and **(h)**, the global circulation is superimposed on the temporally and zonally averaged temperature in the Global Ocean. The contour interval for the circulation is 4 Sv. Thick lines correspond to clockwise circulations whereas dashed lines are for counter-clockwise motions. Upper diagrams show the temporally and zonally averaged meridional wind stress over the ocean.

(2) an intermediate cell representative of the NADW between 40° S and 80° N; (3) a Southern Ocean cell between 40 and 60° S, known as the Deacon Cell and (4) a deep-ocean circulation related to the AABW.

The tropical cells in LGM_E and PD_E are rather similar in extent and intensity (Fig. 2e, f). They recirculate the warmest waters in the upper 500 m of the ocean. In PD_E, they also reorganise the most saline water of the Indo-Pacific basin. In LGM_E, the water of highest salinity is found in the deep ocean. The cell associated with the NADW is shallower in LGM_E than in PD_E (near 1500 m in LGM_E as shown in Fig. 2c, near 2500 m in PD_E as shown in Fig. 2d). The maximum of the AMOC is about 13 Sv at 30°N in each experiment (Table 1). It is located at a depth near 500 m in LGM_E and near 800 m PD_E. The Deacon Cell is found in a region with important tilting of the isotherms and isohalines as shown in Fig. 2a and b. The maximum transport within the Deacon Cell is 28 Sv in LGM_E and 24 Sv in PD_E (Table 1). The 4 Sv difference is due to the larger wind stress over the Southern Ocean surface in LGM_E. Compared to PD_E, the structure of the Southern Ocean zonally averaged temperature and salinity in LGM_E is shifted equatorward due to the larger sea-ice extent, and a larger volume of cold and saline water, originating from the Southern Ocean surface, fills the deep ocean. The zonally averaged isotherms and isohalines in LGM_E are hence slightly shifted equatorward and most of them are concentrated in a thinner surface layer than in PD_E. The Deacon Cell is thus located between 58 and 40° S in LGM_E and penetrates to a depth of about 1000 m whereas it is found between 65 and 38° S and reaches about 4000 m in PD_E. The AABW in PD_E is homogeneous both in temperature and salinity (Fig. 2b and h). It is cold (−2 to 2 °C) and relatively fresh (34.5 to 35 PSU). The associated circulation exports the coldest Southern Ocean surface water down to a depth of 2000 m. The AABW in LGM_E is relatively homogeneous in temperature and the salinity ranges from 35.5 to 37 PSU (Fig. 2a and g). The maximum overturning in the AABW is stronger in LGM_E (19 Sv) than in PD_E (8 Sv). The larger sea-ice extent between 58 and 80° S contributes to maintain the formation of dense AABW in LGM_E. A deep clockwise circulation, between 40° S and the equator, located at a depth of 4000 m, is present in the Indo-Pacific basin and may be the result of a slight meridional density gradient, which is able to sustain a clockwise circulation.

The maximum transport of the AMOC in the Paleoclimate Modelling Intercomparison Project Phase 2 models ranged

between 9 and 12 Sv, while in the AABW it ranged between 5 and 10 Sv. The reduced overturning at high latitudes and the boundary between the NADW and the AABW near 1500 m as simulated in LGM_E agree to a certain extent with the structure simulated by the CCSM3 and Hadl2 simulations (Otto-Bliesner et al., 2007), and particularly to the quasi-equilibrated state simulated by Brandefelt and Otto-Bliesner (2009). These similarities might be a consequence of the atmospheric and oceanic glacial states extracted from the Brandefelt and Otto-Bliesner (2009) simulation and used to force LGM_E. However, the abyssal transport in LGM_E is weak in the North Atlantic and North Pacific compared to the values given by Brandefelt and Otto-Bliesner (2009). This feature might be due to the formation of dense waters in the Southern Ocean that fill the North Atlantic and North Pacific basins, and the difference of bathymetry which prevents the redistribution of the waters between the northern and southern basins through some narrow passages. As a result, homogeneous dense waters are found in the Northern Hemisphere deep basins, which prevent density gradients from maintaining the deep overturning. The sea-ice plays an important role in the water mass formation (Shin et al., 2003; Otto-Bliesner et al., 2007; Zhang et al., 2013). Its impact on the thermohaline regime is identified, for instance, as a factor favouring the densification of the Southern Ocean water in the CCSM3 model (Otto-Bliesner et al., 2007; Brandefelt and Otto-Bliesner, 2009). Similarly, the large sea-ice extent in LGM_E can maintain an expanded and dense AABW coexisting with a shallow NADW. An intensified AABW is also found in the models of Butzin et al. (2005) and Hesse et al. (2011), which include an enhanced northward sea-ice export in the Southern Ocean. This leads to the best agreement for capturing the general ^{13}C distribution (i.e. water masses geometry) derived from sediment analysis.

Paleo-proxy reconstructions agree on a shallower NADW and a larger intrusion of the AABW in the North Atlantic during the LGM (Curry, 2005; Marchitto and Broecker, 2006; Evans and Hall, 2008; Lippold et al., 2012). It has been suggested that the interface between the NADW and the AABW was substantially shallower during the LGM than today. This transition depth between the NADW and the AABW was estimated by Tagliabue et al. (2009) to be around 1750 m, which is very close to the value found in LGM_E (near 1500 m). However, their estimate of the maximum AMOC transport (5 Sv) is weaker than in LGM_E (Table 1). Paleo-proxy reconstructions based on ^{231}Pa / ^{230}Th ratios suggest that the deep circulation during the LGM was stronger or comparable in strength with present-day transports (Yu et al., 1996; Lynch-Stieglitz et al., 2007; Gherardi et al., 2009; Lippold et al., 2012). Other reconstructions based on oxygen-isotope ratios of benthic foraminifera and $\delta^{13}C$ data suggest that the water renewal in the deep ocean was much slower than today (Lynch-Stieglitz et al., 1999; Hesse et al., 2011). Tagliabue et al. (2009) show the transport associated with the AABW in the Atlantic basin is around 4 Sv whereas it is close to 2 Sv in LGM_E (see Table 1). There is also evidence that the deep ocean is homogeneous in temperature during the LGM – near the freezing point in Adkins and Schrag (2001) and between 2 and 4 °C colder than today in Martin et al. (2002). Reconstructions of the abyssal salinity also suggest that the deep ocean was filled with the saltiest water and that the salinity gradient was the main driver of the LGM abyssal circulation (Adkins et al., 2002). The CCSM3 and Hadl2 models (initialised with glacial state) simulate the high salinity in the deep ocean as proposed by Adkins et al. (2002). LGM_E also captures the signature of a cold and extremely saline deep ocean. This might be the consequence of a glacial initial state and the large sea-ice extent which contributes to enhance the formation of saline AABW.

3.1.2 Streamfunction in latitude–tracer coordinates and meridional transports of heat and freshwater

Most cells identified in latitude–depth coordinates are recovered in the latitude–density, the latitude–temperature and the latitude–salinity coordinates. The tropical cells in LGM_E and PD_E are of similar extent (Figs. 3–5). They are mainly associated with the Indo-Pacific circulation. Due to the cold atmospheric condition in LGM_E, the tropical cells are slightly shifted towards colder temperatures than in PD_E (Fig. 4e and f). The maximum transport within the cells is about 10 % larger in LGM_E than in PD_E when one considers the latitude–temperature and latitude–density coordinates (Table 1). As a result, the maximum poleward heat transports near 18° N and 18° S are about 20 % larger in LGM_E (1.5 PW at 18° S and 1 PW at 18° N in Fig. 4e) than in PD_E (Fig. 4f). In each experiment, the freshwater transport associated with the tropical circulation is dominantly directed southwards and the maximum transports are about 0.5 Sv at 10° S and between 0.2 and 0.4 Sv at 34° N.

Important changes in the volume, heat and freshwater transports take place in the Atlantic Ocean and the Southern Ocean. The maximum of the AMOC varies between the coordinate systems. It is larger in PD_E than in LGM_E (see Table 1). The AMOC cell transports mid-latitude warm and saline waters towards higher latitudes, where they become denser (colder) as shown in Fig. 3c and d (Fig. 4c and d). Near 60° N, the waters are transported southward with a near-isopycnal (isothermal and isohaline) transformation and they exit the Atlantic basin near 40° S. Between the equator and 40° N, the transport of heat in the Atlantic basin was about 30 % higher during LGM_E than in PD_E, because the NADW volume transport was stronger during LGM_E and the AABW transport was weaker. Between 40 and 90° N, the meridional heat transport in LGM_E is more than 50 % smaller due to the large sea-ice extent and the Gulf Stream Extension that is constrained into a more zonal propagation between 40 and 45° N. Contrary to density and temperature, salinity is not monotonic in the vertical. As result, the overturning cells in latitude–salinity coordinates will not always correspond to a

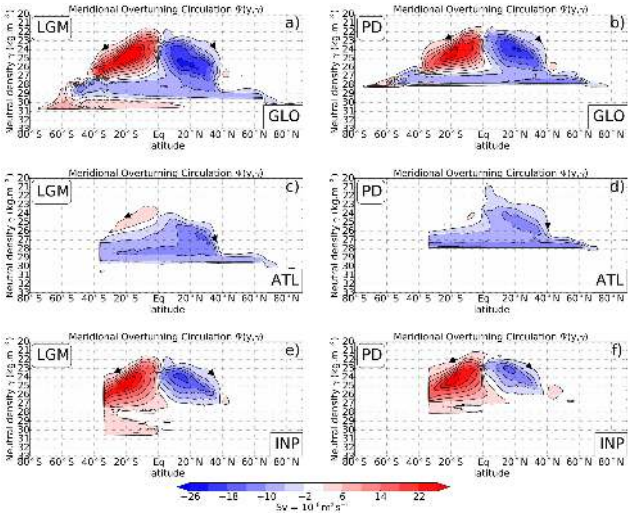

Figure 3. LGM and PD meridional overturning circulation in latitude–neutral density coordinates for **(a, b)** the Global Ocean, **(c, d)** the Atlantic basin and **(e, f)** the Indo-Pacific basin. The contour interval for the circulation is 4 Sv. The blue cells correspond to clockwise circulations whereas the red cells are for counter-clockwise motions.

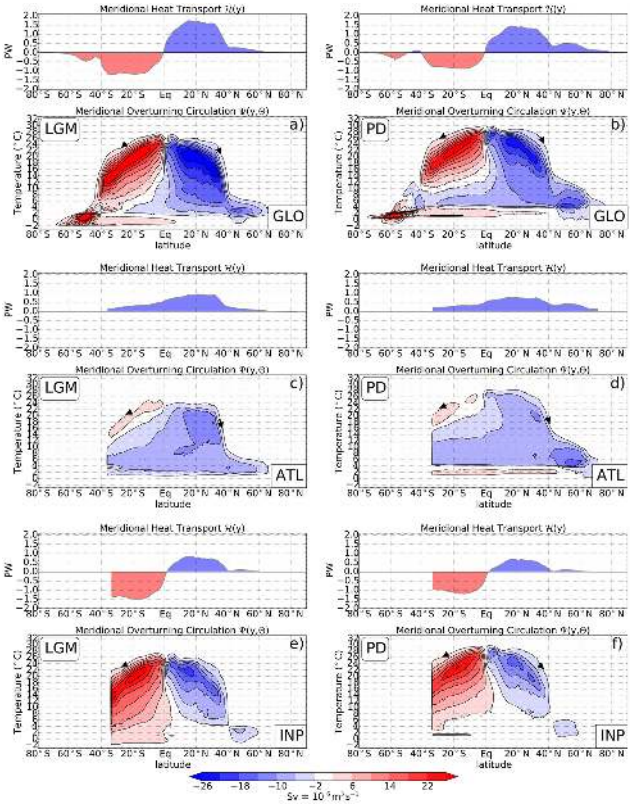

Figure 4. LGM and PD meridional overturning circulation in latitude–temperature coordinates for **(a, b)** the Global Ocean, **(c, d)** the Atlantic basin, and **(e, f)** the Indo-Pacific basin. The contour interval for the circulation is 4 Sv. The blue cells correspond to clockwise circulations whereas the red cells are for counter-clockwise motions. For each basin, the oceanic meridional heat transport in PW is represented.

vertical displacement of a water parcel. However, it becomes useful to study the circulation in latitude–salinity coordinates in the regions where the salinity plays a more important role than the temperature (e.g. polar region) or during a period such as the LGM, when the saline stratification was different than today. In latitude–salinity coordinates, the main differences between LGM_E and PD_E are in the Atlantic basin (Fig. 5c and d). In LGM_E, a large intrusion of saline water originating from the Southern Ocean is found between 40° S and 20° N. This intrusion squeezes and isolates the North Atlantic circulation from the southern part of the Atlantic basin (Fig. 5c). Consequently, the freshwater transport in LGM_E is affected by this change. The freshwater transport is directed northwards between 47° N and the pole, and southwards between 20 and 47° N. This corresponds to the transfers of the mid-latitude freshwater (see Fig. S5 in the Supplement) by the North Atlantic and sub-polar gyres. Between 37° S and 20° N, the freshwater transport in LGM_E is directed northwards, associated with waters originating from the South Pole. In PD_E, between 20 and 90° N, it is directed southwards, representing the transfer of freshwater from the pole to the mid-latitudes.

Compared to the averaging in latitude–depth coordinates, the circulation associated with the Deacon Cell is reduced by about 40 % in latitude–density (Fig. 3a and b) and by more than 60 % in latitude–temperature coordinates (Fig. 4a and b). In latitude–salinity coordinates, the maximum overturning is similar as in latitude–depth coordinates (Fig. 5a and b). The abyssal waters are denser in the LGM_E than in PD_E (Fig. 3a) because of the larger salinities at depth. In PD_E, the abyssal overturning is nearly along the 28.1 kg m^{-3} neutral density surface because the abyssal ocean is homogeneous in density. The overturning associated with the AABW consists of a near-isothermal transport of the coldest waters in latitude–temperature coordinates. The abyssal circulation in the Atlantic Ocean in LGM_E is extremely weak in latitude–temperature coordinates due to the weak thermal stratification below 1000 m. In latitude–temperature coordinates, a closed circulation centred near 50° S in LGM_E and 60° S in PD_E is associated with the surface overturning (Fig. 4a and b). In this region, the transports of heat in LGM_E and PD_E are similar (about 0.5 PW) and directed towards Antarctica. The deep overturning in LGM_E is also characterised by a circulation of saline waters ranging from 36 to 37 PSU, which maintains a maximum overturning of 6 Sv near 60° S. Associated with this overturning about 0.3 Sv of freshwater are transported towards Antarctica.

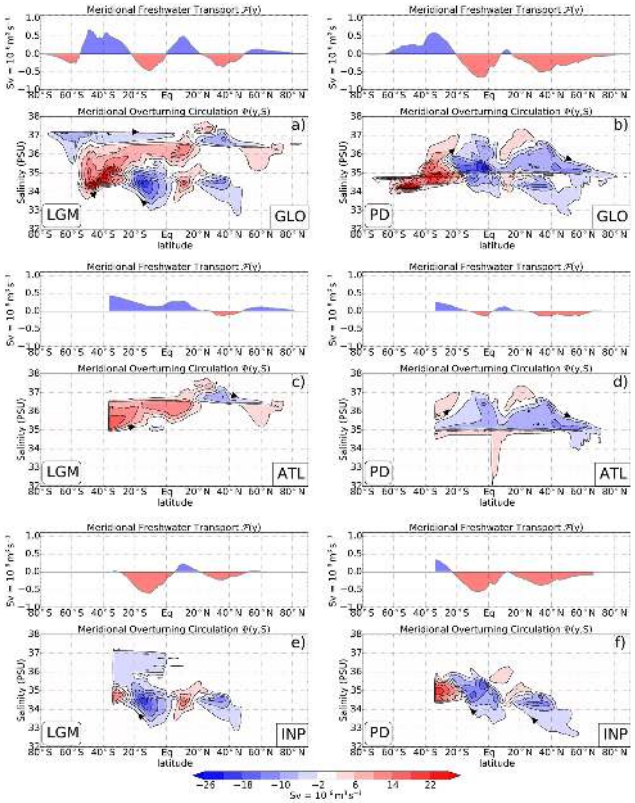

Figure 5. LGM and PD meridional overturning circulation in latitude–salinity coordinates for **(a, b)** the Global Ocean, **(c, d)** the Atlantic basin, and **(e, f)** the Indo-Pacific basin. The contour interval for the circulation is 4 Sv. The blue cells correspond to clockwise circulations whereas the red cells are for counter-clockwise motions. For each basin, the oceanic meridional freshwater transport in Sv is represented.

3.2 Transports in thermohaline coordinates

This section presents the THC in thermohaline coordinates, the volumetric distribution in the θ–S diagram and an estimate of the timescale of the circulation.

3.2.1 Thermohaline streamfunction and transport of heat/freshwater in temperature and salinity coordinates

The ocean circulation in thermohaline coordinates consists of three main cells (Fig. 6a, b): (i) a tropical cell, which reflects the water mass transformation in the upper near-equatorial Pacific; (ii) a Conveyor Belt cell, which is the dominant circulation in the diagram and captures the inter-ocean transport of heat and salt; and (iii) a low-temperature cell which corresponds to the AABW.

The tropical cell in PD_E is centred at 35 PSU and 27 °C and has a maximum transport of 21 Sv. It corresponds to the shallow wind-driven transport (equatorial undercurrent in the central Pacific). It converts the 33.5 to 35 PSU water-masses into more saline (35 to 37 PSU) water-masses (or the 21 to 27 °C water-masses into warmer 27 to 30 °C water-masses). The tropical cell in LGM_E is shifted towards colder isotherms and fresher isohalines due to the cold conditions and reduced evaporation at the surface. It is hence centred at 34.5 PSU and 24 °C and has a maximum transport of 24 Sv. It converts the 31 to 34.5 PSU water-masses into more saline (34.5 to 35.5 PSU) water-masses (or the 16 to 24 °C water-masses into warmer, 24 to 28 °C, water-masses). The water cycle in the tropics can be described as follow (see the schematic Fig. 7): (a) the conversion is almost isothermal toward lower salinities near 27 °C corresponding to the freshening of the surface waters at the surface of the western Pacific pool, where the net precipitation and the surface heat flux is weak; (b) the surface waters flow polewards and becomes cooler and more saline; (c) a transformation where the net evaporation and the heat flux are strong in the eastern equatorial Pacific. This latter transformation is nearly isohaline along the 34.6 PSU isohaline in LGM_E. The maximum heat transport carried by the tropical cell is 0.5 PW in LGM_E. In PD_E, the maximum transport of heat is half as strong during LGM_E. The maximum freshwater transports are rather similar between PD_E and LGM_E. The tropical cell transports about 1 Sv near the 25 °C isotherm in LGM_E and near the 28 °C in PD_E.

The large-scale transport in the Conveyor Belt cell (e.g. the transport between the −2 and −6 Sv streamlines in Fig. 6) is similar to the Broecker (1991) loop and can be described as follows (see the water cycle illustrated in the schematic of Fig. 7):

1. the Indo-Pacific surface-waters ($16\,°C \leq \theta \leq 22\,°C$ and $34.5\,PSU \leq S \leq 35\,PSU$) become colder approaching Cape Agulhas and enter the South Atlantic basin ($S \approx 35$ PSU); these waters flow northward and increase their salinity and temperature;

2. the waters cool near 36.5–37 PSU, become fresher (between $\sigma_0 = 28\,kg\,m^{-3}$ and $\sigma_0 = 29\,kg\,m^{-3}$ in LGM_E, and between $\sigma_0 = 27\,kg\,m^{-3}$ and $\sigma_0 = 28\,kg\ m^{-3}$ in PD_E);

3. they sink to the deep ocean;

4. finally they upwell in the North Pacific basin as cold and fresh waters.

Smaller-scale transformations exist in the Indo-Pacific and Southern Oceans. For instance, the maximum volume transport in LGM_E takes place near the 34.1 PSU isohaline and is about 20.2 Sv. In PD_E, the volume transport has a maximum near the 34.7 PSU isohaline with a magnitude of 23.6 Sv. These circulations are associated with the intense transports in the ACC and the formation of the Antarctic Intermediate Water. The shape of the Conveyor Belt cell differs between the two experiments. In LGM_E, the Conveyor Belt Cell occupies more isohaline layers than in PD_E since the Atlantic

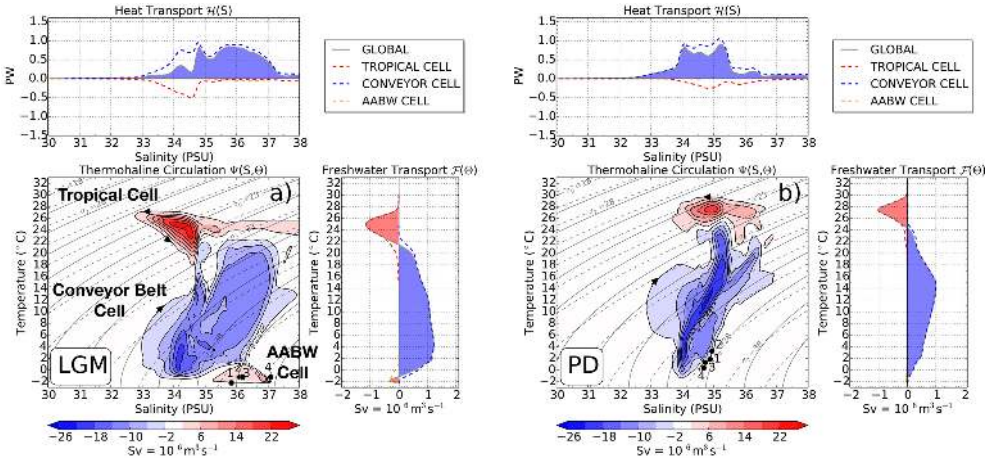

Figure 6. Thermohaline streamfunction computed for **(a)** the LGM simulation and **(b)** the PD simulation. The contour interval for the circulation is 4 Sv. The blue cells correspond to clockwise circulations whereas the red cells are for counter-clockwise motions. The upper diagram correspond to the oceanic heat transport within each isohaline is plotted. The left diagram shows the freshwater transport within each isotherm. The black dots represent the deep ocean temperature and salinity from Adkins et al. (2002): 1: Bermuda Rise, 2: Feni Drift, 3: Chatham Rise, 4: Shona Rise.

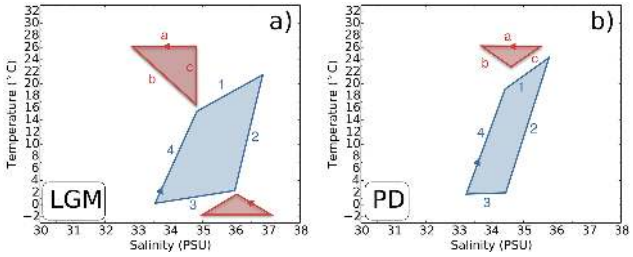

Figure 7. Schematic illustration of the water cycle in the various thermohaline cells.

thermohaline regime is changed. A near-isothermal transformation (near 22 °C) appears in the Atlantic basin. It corresponds to the inter-tropical surface circulation driven by the strong salinity contrast between the North and South Atlantic basins in LGM_E (see Fig. 2c). This is not observed in PD_E which is mainly driven by a difference in temperature rather than the difference in salinity (Fig. 6b). These reorganisations modify the transports of heat and freshwater. In PD_E, a maximum freshwater transport of 1 Sv is found between the 14 and 16 °C isotherms and the maximum heat transport (about 1 PW) is between the 34 and 35.5 PSU isohalines (associated with the Indo-Pacific and Atlantic basins heat transports). In LGM_E, the Conveyor Belt Cell carries a maximum of 1.2 Sv of freshwater along the 4 °C isotherm and the heat transport is more spread between the 35 and 37 PSU isohalines.

The AABW cell is particularly strong in LGM_E due to the greater saline stratification in the abyss (Fig. 6a). It also captures the LGM hydrography derived by Adkins et al. (2002). In PD_E, this cell is small (centred at 34.7 PSU and 1 °C) because the modern deep ocean is relatively homogeneous in temperature and salinity (Fig. 6b). Hence, the low-temperature cell in PD_E does not participate significantly in the global transport of heat and freshwater. On the contrary, the freshwater transport associated with the low-temperature cell in LGM_E reaches a maximum of about 0.4 Sv along the −2 °C isotherm.

3.2.2 Volumetric distribution in the T–S diagram

The different thermohaline regimes between LGM_E and PD_E can be illustrated by the sea-water volume density in the temperature-salinity diagram (Fig. 8). In LGM_E, the maximum volume density of sea-water is found for relatively cold and saline waters. The temperatures are between −2 and 0 °C, and the salinities vary between 36.5 and 37.5 PSU. For the intermediate waters (i.e. between 2 and 16 °C), the volume density of sea-water greater than 10^{14} m^3 °C^{-1} PSU^{-1} is found in two "branches": the waters with salinity between 36 and 37 PSU associated with the Atlantic waters, and the relatively fresher waters between 34 and 36 PSU, corresponding to the Indo-Pacific waters (see Fig. S4 in the Supplement and Fig. 5 for the distinction between the Atlantic and Pacific "branches"). These two branches are not as distinct in PD_E, suggesting that the Atlantic and the Indo-Pacific basins have a tighter thermohaline structure under the present-day conditions than for the LGM period. The distinct signature of the Atlantic and Pacific waters in LGM_E might be a consequence of the reduced connection at the Agulhas leakage between the Indian and Atlantic basin as shown with the barotropic streamfunction (Fig. 1a). Contrary to PD_E, the Conveyor Belt cell in LGM_E is also less connected to the deep ocean. This is due to a larger abyssal circulation which tends to lift and deviate the Conveyor Belt cell from the area of maximum volumetric density.

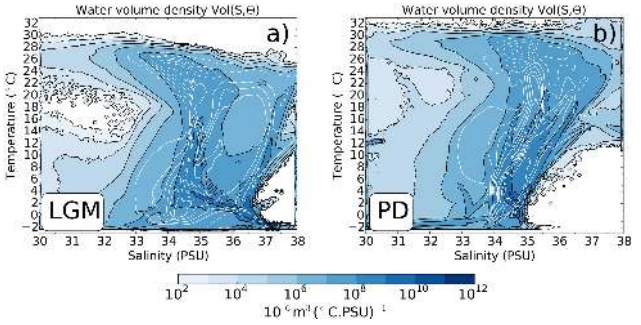

Figure 8. Sea-water volume density distribution projected in the temperature–salinity diagram for **(a)** the LGM simulation and **(b)** the PD simulation. The LGM and PD thermohaline streamfunctions are superimposed. The contour interval for the volume density is 10^6 m^{-3} (°C PSU)$^{-1}$. The volume density at $S = 30$ PSU and $S = 38$ PSU includes volume density of water with $S \leq 30$ PSU and $S \geq 38$ PSU, respectively.

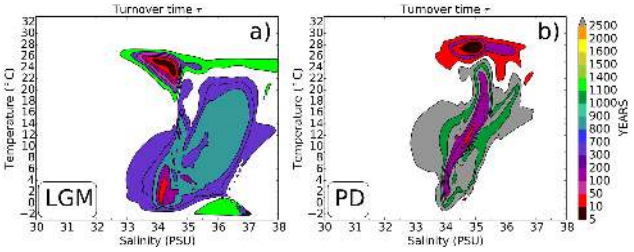

Figure 9. Turnover times (in years) in each stream layer of the thermohaline streamfunction computed for the **(a)** LGM simulation and **(b)** the PD simulation.

3.2.3 Turnover times

For each simulation, the shortest turnover times (see Appendix A3.2) are found in the tropical cell (Fig. 9). The length of time spent in the cells can differ widely between two successive layers because of the different lengths of the circuits in the layers. In PD_E, the turnover times in the Conveyor Belt cell vary between 50 years (where the water conversion is at a minimum) and more than 2500 years (for the global-scale transports). In LGM_E, the times in the Conveyor Belt cell are shorter (between 50 and 800 years). In the cell representative of the AABW, the times are between 50 and 1000 years in LGM_E, representing the rapid sinking of the water near the surface and the large-scale slow motion in the abyss. The large volume of AABW explains the reduced ventilation of the deep ocean and the associated large turnover time. These larger residence times for the AABW are consistent with the times derived from paleo-proxy reconstructions based on radiocarbon and oxygen isotopic ratio (Keigwin, 2004; Lund et al., 2011). In PD_E, the turnover time for the circulation in the AABW is around 50 years, corresponding to the rapid sinking of the surface circulation near Antarctica. The rest of the AABW circulation is weak in this diagram and therefore not captured by the thermohaline streamfunction.

4 Conclusions

The morphology of the thermohaline circulation during the LGM and the present day is herein presented from numerical experiments and streamfunctions projected in various coordinate systems. We found that important changes between the LGM and the present-day THC take place in the Atlantic basin, the Southern Ocean and in the abyss which are consistent with paleo-proxy reconstructions. In comparison to the present day, the mean thermocline depth is shallower during the LGM. Below this thermocline, the ocean is filled with the most saline waters originating from the Southern Ocean. Near the surface, the volume transports are about 10 % larger in the tropical cells due to the larger surface wind stress. Consequently, the maximum transport of heat in the tropics is between 15 to 25 % larger during the LGM. The Gulf Stream has a more zonal propagation, reducing the heat transport at high latitudes by almost 50 %. The AMOC is shallower but its strength is similar to the present day. The circulation in the AABW cell is more vigorous in the Southern Ocean and occupies more volume than under present-day conditions. In the North Pacific and North Atlantic basins, the deep circulation is almost sluggish due to the weak meridional density gradients.

The circulations in latitude–salinity and thermohaline coordinates illustrate the different haline regimes between the glacial and the interglacial periods. They also highlight the Atlantic and Southern oceans as regions of important rearrangement. The thermohaline structure in LGM_E is represented by an abyssal circulation which lifts and makes the Conveyor Belt cell deviate from the area of maximum volumetric density. The LGM THC is thus represented by a ventilated upper layer above a deep stagnant layer as shown by the turnover times in the different thermohaline cells. The shorter travel time in the LGM Conveyor Belt can be explained by a combination of the vigorous surface circulation for the LGM, the shorter route of the near-surface circulation and a circulation associated with the AABW that squeezes most of the Conveyor Belt cell in a shallower part of the ocean. The turnover time of the glacial abyssal circulation is large, suggesting a nearly sluggish circulation.

The present study shows that the maximum transport of volume, heat and freshwater by the main ocean overturning cells depend strongly on the choice of coordinate system. For instance, the maximum of the AMOC varies between 9 and 16 Sv during the LGM, and between 12 to 19 Sv for the present day. The new thermohaline streamfunction is a powerful tool of analysis to investigate and summarise the thermohaline structure between different model integrations. It also allows us to estimate the timescales (turnover

times) of the ocean water cycles. The changes in the ocean thermohaline regime between the LGM and the present day raise some interesting questions about the ocean's role for controlling the atmospheric CO_2 between glacial and interglacial period. In a climate change context, one might also ask whether the representation of the THC in multiple coordinate systems, as considered here, might more clearly reveal important changes under future climate scenarios with increased greenhouse gas forcing? Would the pace of the THC increase or decrease? What would then be the impact on the oceanic transport of heat and freshwater as well as on the carbon cycle?

Appendix A: Mathematical formulation of the streamfunctions

A1 Transport in geographical coordinates

A1.1 Barotropic streamfunction

The barotropic streamfunction is the vertically integrated volume transport in Sv ($\equiv 10^6\,\mathrm{m^3\,s^{-1}}$) at a given location (Eq. A1). It yields the averaged circulation in the horizontal plane:

$$\Psi(x,y) = \frac{1}{t_1-t_0}\int_{t_0}^{t_1}\int_{y_S}^{y}\int_{-H}^{\eta}(U(x,y,z',t) + U_{\mathrm{eddy}}(x,y,z',t))\mathrm{d}z'\mathrm{d}y\mathrm{d}t. \quad \text{(A1)}$$

Here x, y, z' are the zonal, meridional and vertical coordinates, t is the time, t_1-t_0 the time interval for the averaging, y_S the southern boundary (Antarctica), H the depth of the water column, η the sea surface elevation, U and U_{eddy} the zonal velocity and the eddy-induced velocity.

The barotropic streamfunctions in $\mathrm{LGM_E}$ and $\mathrm{PD_E}$ are shown in Fig. 1.

A2 Meridional overturning circulation in latitude–depth coordinates

The streamfunction in latitude–depth coordinates is, at a given latitude, the volume transports in Sv ($\equiv 10^6\,\mathrm{m^3\,s^{-1}}$) in the water column (Eq. A2):

$$\Psi(y,z) = \frac{1}{t_1-t_0}\int_{t_0}^{t_1}\int_{x_E}^{x_W}\int_{-H}^{z}(V(x,y,z',t) + V_{\mathrm{eddy}}(x,y,z',t))\mathrm{d}z'\mathrm{d}x\mathrm{d}t. \quad \text{(A2)}$$

Here x, y, z' are the zonal, meridional and vertical coordinates, t is the time, t_1-t_0 the time interval for the averaging, z the depth, x_E and x_W the eastern and western boundaries, H the depth of the water column, V and V_{eddy} the meridional velocity and the eddy-induced velocity.

The MOC in latitude–depth coordinates in $\mathrm{LGM_E}$ and $\mathrm{PD_E}$ are shown in Fig. 2 for the Global Ocean, the Atlantic Ocean and the Indo-Pacific basin.

A2.1 Meridional overturning circulation in latitude–density coordinates

The streamfunction in latitude–density coordinates is, at a given latitude, the volume transport in Sv ($\equiv 10^6\,\mathrm{m^3\,s^{-1}}$) within an isopycnal (Eq. A3):

$$\Psi(y,\gamma) = \frac{1}{t_1-t_0}\int_{t_0}^{t_1}\int_{x_E}^{x_W}\int_{-H}^{z(x,y,\gamma,t)}(V(x,y,z',t) + V_{\mathrm{eddy}}(x,y,z',t))\mathrm{d}z'\mathrm{d}x\mathrm{d}t. \quad \text{(A3)}$$

Here x, y, z' are the zonal, meridional and vertical coordinates, t is the time, t_1-t_0 the time interval for the averaging, γ the neutral density, $z(x,y,\gamma,t)$ the depth of the neutral density surface γ, x_E and x_W the eastern and western boundaries, V and V_{eddy} the meridional velocity and the eddy-induced velocity contribution.

The Meridional overturning circulation (MOC) in latitude–density coordinates in $\mathrm{LGM_E}$ and $\mathrm{PD_E}$ are shown in Fig. 3 for the Global Ocean, the Atlantic Ocean and the Indo-Pacific basin.

A2.2 Meridional overturning circulation in latitude–temperature coordinates and the transport of heat

The streamfunction in latitude–temperature coordinates is, at a given latitude, the volume transport in Sv ($\equiv 10^6\,\mathrm{m^3\,s^{-1}}$) within an isotherm (Eq. A4):

$$\Psi(y,\theta) = \frac{1}{t_1-t_0}\int_{t_0}^{t_1}\int_{x_E}^{x_W}\int_{-H}^{z(x,y,\theta,t)}(V(x,y,z',t) + V_{\mathrm{eddy}}(x,y,z',t))\mathrm{d}z'\mathrm{d}x\mathrm{d}t. \quad \text{(A4)}$$

Here x, y, z' are the zonal, meridional and vertical coordinates, t is the time, t_1-t_0 the time interval for the averaging, θ the temperature, $z(x,y,\theta,t)$ the depth of the isothermal surface θ, x_E and x_W the eastern and western boundaries, V and V_{eddy} the meridional velocity and the eddy-induced velocity.

The integral of the transports along each isotherm at a given latitude is an estimate of the advective meridional heat transport in PetaWatt (PW) $= 10^{15}$W (Eq. A5). A positive heat transport is a transport towards the North Pole, a negative transport is towards the south pole:

$$\mathcal{H}(y) = \int_{\theta_{\min}}^{\theta_{\max}}\rho C_p\Psi(y,\theta)\mathrm{d}\theta. \quad \text{(A5)}$$

Here y is the latitude, θ the temperature, $\theta_{\max}$ and $\theta_{\min}$ the maximum and minimum temperatures considered, $\rho = 1035\,\mathrm{kg\,m^{-3}}$ the average density of seawater and $C_p \approx 4000\,\mathrm{J\,(kg\,^\circ C)^{-1}}$ the specific heat for seawater.

The MOC in latitude–temperature coordinates in $\mathrm{LGM_E}$ and $\mathrm{PD_E}$ are shown in Fig. 4 for the Global Ocean, the Atlantic Ocean and the Indo-Pacific basin.

A2.3 Meridional overturning circulation in latitude–salinity coordinates and the transport of freshwater

The streamfunction in latitude–salinity coordinates is, at a given latitude, the volume transport in Sv ($\equiv 10^6\,\mathrm{m^3\,s^{-1}}$) within isohalines (Eq. A6):

$$\Psi(y,S) = \frac{1}{t_1 - t_0}\int_{t_0}^{t_1}\int_{x_E}^{x_W}\int_{-H}^{z(x,y,S,t)} (V(x,y,z',t) + V_{\mathrm{eddy}}(x,y,z',t))\mathrm{d}z'\mathrm{d}x\mathrm{d}t. \quad \text{(A6)}$$

Here x, y, z' are the zonal, meridional and vertical coordinates, t is the time, $t_1 - t_0$ the time interval for the averaging, S the salinity, $z(x,y,S,t)$ the depth of the isohaline surface S, x_E and x_W the eastern and western boundaries, V and V_{eddy} the meridional velocity and the eddy-induced velocity.

The integral of the transports along each isohaline at a given latitude is an estimation of the meridional freshwater transport in Sv (Eq. A7). The positive and negative freshwater transport is a transport towards the north pole and towards the South Pole, respectively:

$$\mathcal{F}(y) = \int_{S_{\min}}^{S_{\max}} \frac{\Psi(y,S)}{S_{\mathrm{r}}}\mathrm{d}S. \quad \text{(A7)}$$

Here y is the latitude, S the salinity, $S_{\max}$ and $S_{\min}$ the maximum and minimum salinities considered, and $S_{\mathrm{r}} = 35$ PSU is a constant reference salinity.

The MOC in latitude–salinity coordinates and the associated transports of freshwater in $\mathrm{LGM_E}$ and $\mathrm{PD_E}$ are shown in Fig. 5.

A3 Transport in thermohaline coordinates

A3.1 Thermohaline streamfunction and transport of heat/freshwater in temperature and salinity coordinates

The thermohaline streamfunction (Eq. A8) is the volume transport in Sv ($\equiv 10^6\,\mathrm{m^3\,s^{-1}}$) brought about by the temperature and the salinity differences between the World Ocean basins (Döös et al., 2012; Zika et al., 2012). This representation has the advantage of taking into account the three-dimensional aspect of the ocean circulation. It also captures the transports and the parameters of state (temperature and salinity) of the ocean water parcels. The representation has however the disadvantage of removing the geographical coordinates. It is defined as follows:

$$\Psi(S,\theta) = \frac{1}{t_1 - t_0}\int_{t_0}^{t_1}\int_{\mathrm{Ath}\,(S,\theta)} (\boldsymbol{V} + \boldsymbol{V}_{\mathrm{eddy}})\mathrm{d}\boldsymbol{A}\mathrm{d}t. \quad \text{(A8)}$$

Here $t_1 - t_0$ is the time interval for the averaging, $\mathrm{Ath}\,(S,\theta)$ is the part of the isothermal surface θ where the salinity is less than S, $\boldsymbol{V}$ and $\boldsymbol{V}_{\mathrm{eddy}}$ are the three-dimensional Eulerian and eddy-induced velocity vectors, and $\mathrm{d}\boldsymbol{A}$ is the element surface on $\mathrm{Ath}\,(S,\theta)$ pointing towards increasing temperature.

Using this representation allows us to evaluate the transport of heat in PW within a specific isohaline range (Eq. A9) as well as the transport of freshwater in Sv within specific isotherm (Eq. A10). These diagnostics can be applied for understanding the oceanic reorganisations under different climate conditions and for comparing or validating different model integrations. A positive heat transport is a transport towards increasing salinity and vice versa for negative transport values. Similarly, a positive freshwater transport is a transport from cold to warm waters:

$$\mathcal{H}(S) = -\rho C_p \int_{\theta_{\min}}^{\theta_{\max}} \Psi(S,\theta)\mathrm{d}\theta. \quad \text{(A9)}$$

Here S is the salinity, θ the temperature, $\rho = 1035\,\mathrm{kg\,m^{-3}}$ the average density of seawater and $C_p = 4000\,\mathrm{J\,(kg\,^\circ C)^{-1}}$ the specific heat for seawater, $\theta_{\min}$ and $\theta_{\max}$ the minimum and maximum temperature considered:

$$\mathcal{F}(\theta) = -\int_{S_{\min}}^{S_{\max}} \frac{(\Psi(S,\theta))}{S_{\mathrm{r}}}\mathrm{d}S. \quad \text{(A10)}$$

Here θ is the temperature, S is the salinity, and $S_r = 35$ PSU is a constant reference salinity, $S_{\min}$ and $S_{\max}$ the minimum and maximum salinity considered.

The thermohaline streamfunction and the associated heat and freshwater transports in $\mathrm{LGM_E}$ and $\mathrm{PD_E}$ are shown in Fig. 6. We assume that the tracers are in a steady state, i.e. the drifts are small.

A3.2 Turnover time

The thermohaline streamfunction and the volumetric distribution in the temperature-salinity diagram makes possible an estimate of the turnover time τ (Eq. A11) in each stream layer (Döös et al., 2012). In a steady-state climate, it is the ratio of the volume of sea-water (in $\mathrm{m^3}$) between two successive streamlines $V(\Delta\Psi)$ to the corresponding volume transport V (in Sv $\equiv 10^6\,\mathrm{m^3\,s^{-1}}$) between the streamlines:

$$\tau(\Delta\Psi) = \frac{V(\Delta\Psi)}{\Delta\Psi}. \quad \text{(A11)}$$

The turnover times for $\mathrm{LGM_E}$ and $\mathrm{PD_E}$ are shown in Fig. 9.

The Supplement related to this article is available online at doi:10.5194/os-11-907-2014-supplement.

Acknowledgements. This work has been financially supported by the Bert Bolin Centre for Climate Research and by the Swedish Research Council. The Swedish National Infrastructure for Computing (SNIC) is gratefully acknowledged for providing the computer resources on the Vagn and Ekman facilities funded by the Knut and Alice Wallenberg Foundation. We would like to thank three anonymous reviewers for their constructive comments on the paper.

Edited by: M. Hecht

References

Adkins, J. F. and Schrag, D. P.: Pore fluid constraints on deep ocean temperature and salinity during the Last Glacial Maximum, Geophys. Res. Lett., 28, 771–774, doi:10.1029/2000GL011597, 2001.

Adkins, J. F., Mcintyre, K., and Schrag, D. P.: The Salinity, Temperature, and δ^{18}O of the Glacial Deep Ocean, Science, 298, 1769–1773, doi:10.1126/science.1076252, 2002.

Ballarotta, M., Brodeau, L., Brandefelt, J., Lundberg, P., and Döös, K.: Last Glacial Maximum world ocean simulations at eddy-permitting and coarse resolutions: do eddies contribute to a better consistency between models and palaeoproxies?, Clim. Past, 9, 2669–2686, doi:10.5194/cp-9-2669-2013, 2013a.

Ballarotta, M., Brodeau, L., Brandefelt, J., Lundberg, P., and Döös, K.: A Last Glacial Maximum world-ocean simulation at eddy-permitting resolution – Part 1: Experimental design and basic evaluation, Clim. Past Discuss., 9, 297–328, doi:10.5194/cpd-9-297-2013, 2013b.

Barnier, B., Madec, G., Penduff, T., Molines, J. M., Tréguier, A. M., Le Sommer, J., Beckmann, A., Biastoch, A., Böning, C., Dengg, J., Derval, C., Durand, E., Gulev, S., Remy, E., Talandier, C., Theetten, S., Maltrud, M., McClean, J., and De Cuevas, B.: Impact of partial steps and momentum advection schemes in a global ocean circulation model at eddy-permitting resolution, Ocean Dynam., 56, 543–567, doi:10.1007/s10236-006-0082-1, 2006.

Barnier, B., Brodeau, L., LeSommer, J., Molines, J.-M., Penduff, T., Theetten, S., Tréguier, A.-M., Madec, G., Biastoch, A., Böning, C., Dengg, J., Gulev, S., Bourdallé, B. R., Chanut, J., Garric, G., Coward, A., de Cuevas, B., New, A., Haines, K., Smith, G. C., Drijfhout, S., Hazeleger, W., Severijns, C., and Myers, P.: Eddy-permitting Ocean Circulation Hindcasts Of Past Decades, CLIVAR Exchanges, 12, 8–10, 2007.

Blanke, B., Arhan, M., and Speich, S.: Salinity changes along the upper limb of the Atlantic thermohaline circulation, Geophys. Res. Lett., 33, L06609, doi:10.1029/2005GL024938, 2006.

Bryan, F. O., Danabasoglu, G. Nakashiki, N., Yoshida, Y., Kim, D. H., Tsutsui, J., and Doney, S. C.: Response of the North Atlantic Thermohaline Circulation and Ventilation to Increasing Carbon Dioxide in CCSM3, J. Climate, 19, 2382–2397, doi:10.1175/JCLI3757.1, 2006.

Brandefelt, J. and Otto-Bliesner, B. L.: Equilibration and variability in a Last Glacial Maximum climate simulation with CCSM3, Geophys. Res. Lett., 36, 1–5, doi:10.1029/2009GL040364, 2009.

Brodeau, L. Barnier, B., Tréguier, A. M., Penduff, T., and Gulev, S.: An ERA40-based atmospheric forcing for global ocean circulation models, Ocean Model., 31, 88–104, doi:10.1016/j.ocemod.2009.10.005, 2010.

Broecker, W. S.: The great ocean conveyor, Oceanography, 4, 79–89, 1991.

Butzin, M., Prange, M., and Lohmann, G.: Radiocarbon simulations for the glacial ocean: The effects of wind stress, Southern Ocean sea ice and Heinrich events, Earth Planet. Sc. Lett., 235, 45–61, doi:10.1016/j.epsl.2005.03.003, 2005.

Curry, W. B.: Glacial water mass geometry and the distribution of δ^{13}C of ΣCO_2 in the western Atlantic Ocean, Paleoceanography, 20, 1–13, doi:10.1029/2004PA001021, 2005.

Döös, K., Meier, M., and Döscher, R.: The Baltic haline conveyor belt or the overturning circulation and mixing in the Baltic, Ambio, 33, 261–266, doi:10.1579/0044-7447-33.4.261, 2004.

Döös, K. and Webb, D.: The Deacon Cell and the other meridional cells of the Southern Ocean, J. Phys. Oceanogr., 24, 429–442, 1994.

Döös, K., Nilsson, J., Nycander, J., Brodeau, L., and Ballarotta, M.: The World Ocean Thermohaline Circulation, J. Phys. Oceanogr., 42, 1445–1460, doi:10.1175/JPO-D-11-0163.1, 2012.

Dufresne, J.-L., Foujols, M.-A., Denvil, S., Caubel, A., Marti, O., Aumont, O., Balkanski, Y., Bekki, S., Bellenger, H., Benshila, R., Bony, S., Bopp, L., Braconnot, P., Brockmann, P., Cadule, P., Cheruy, F., Codron, F., Cozic, A., Cugnet, D., de Noblet, N., Duvel, J.-P., Ethé, C., Fairhead, L., Fichefet, T., Flavoni, S., Friedlingstein, P., Grandpeix, J.-Y., Guez, L., Guilyardi, E., Hauglustaine, D., Hourdin, F., Idelkadi, A., Ghattas, J., Joussaume, S., Kageyama, M., Krinner, G., Labetoulle, S., Lahellec, A., Lefebvre, M.-P., Lefevre, F., Levy, C., Li, Z. X., Lloyd, J., Lott, F., Madec, G., Mancip, M., Marchand, M., Masson, S., Meurdesoif, Y., Mignot, J., Musat, I., Parouty, S., Polcher, J., Rio, C., Schulz, M., Swingedouw, D., Szopa, S., Talandier, C., Terray, P., Viovy, N., and Vuichard, N.: Climate change projections using the IPSL-CM5 Earth System Model: from CMIP3 to CMIP5, Clim. Dynam., 40, 2123–2165, doi:10.1007/s00382-012-1636-1, 2013.

Evans, H. K. and Hall, I. R.: Deepwater circulation on Blake Outer Ridge (western North Atlantic) during the Holocene, Younger Dryas, and Last Glacial Maximum, Geochem. Geophy. Geosy., 9, Q03023, doi:10.1029/2007GC001771, 2008.

Fichefet, T. and Morales Maqueda, M. A.: Sensitivity of a global sea ice model to the treatment of ice thermodynamics and dynamics, J. Geophys. Res., 102, 12609–12646, doi:10.1029/97JC00480, 1997.

Ferrari, R. and Ferreira, D.: What processes drive the ocean heat transport?, Ocean Model., 38, 171–1866, doi:10.1016/j.ocemod.2011.02.013, 2011.

Ganachaud, A. and Wunsch, C.: Improved estimates of global ocean circulation, heat transport and mixing from hydrographic data, Nature, 408, 453–457, 2000.

Gent, P. R. and McWilliams, J. C.: Isopycnal mixing in Ocean Circulation models, J. Phys. Oceanogr., 20, 150–155, doi:10.1175/1520-0485(1990)020<0150:IMIOCM>2.0.CO;2, 1990.

Gherardi, J. M., Labeyrie, L., Nave, S., Francois, R., McManus, J. F., and Cortijo, E.: Glacial-interglacial circulation changes inferred from $^{231}Pa/^{230}Th$ sedimentary record in the North Atlantic region, Paleoceanography, 24, 1–14, doi:10.1029/2008PA001696, 2009.

Grist, J. P., Josey, S. A., and Marsh, R.: Surface estimates of the Atlantic overturning in density space in an eddy-permitting ocean model, J. Geophys. Res., 117, C06012, doi:10.1029/2011JC007752, 2012.

Gruber, N., Gloor, M., Mikaloff Fletcher, S. E., Doney, S. C., Dutkiewicz, S., Follows, M. J., Gerber, M., Jacobson, A. R., Joos, F., Lindsay, K., Menemenlis, D., Mouchet, A., Müller, S. A., Sarmiento, J. L., and Takahashi, T.: Oceanic sources, sinks, and transport of atmospheric CO_2, Global Biogeochem. Cy., 23, GB1005, doi:10.1029/2008GB003349, 2009.

Hazeleger, W.: EC-Earth: A Seamless Earth System Prediction Approach in Action, B. Am. Meteorol. Soc., 3, 1357–1363, doi:10.1175/2010BAMS2877.1, 2010.

Hesse, T., Butzin, M. Bickert, T., and Lohmann, G.: A model-data comparison of $\delta^{13}C$ in the glacial Atlantic Ocean, Paleoceanography, 26, PA3220, doi:10.1029/2010PA002085, 2011.

Hirst, A., Jackett, D., and McDougall, T.: The meridional overturning cells of a world ocean model in neutral density coordinates, J. Phys. Oceanogr., 26, 775–791, 1996

Jackett, D. and McDougall, T. J.: Minimal adjustment of hydrostatic profiles to achieve static stability, J. Atmos. Ocean. Tech., 12, 381–389, doi:10.1175/1520-0426(1995)012<0381:MAOHPT>2.0.CO;2, 2003.

Knight, J. R., Allan, R. J., Folland, C. K., Vellinga, M., and Mann, M. E.: Ocean ventilation and sedimentation since the glacial maximum at 3 km in the western North Atlantic, Geochem. Geophy. Geosys., 3, doi:10.1029/2001GC000283, 2002.

Keigwin, L. D.: Radiocarbon and stable isotope constraints on Last Glacial Maximum and Younger Dryas ventilation in the western North Atlantic, Paleoceanography, 19, PA4012, doi:10.1029/2004PA001029, 2004.

Knight, J. R., Allan, R. J., Folland, C. K., Vellinga, M., and Mann, M. E.: A signature of persistent natural thermohaline circulation cycles in observed climate, Geophys. Res. Lett., 32, L20708, doi:10.1029/2005GL024233, 2005.

Lee, M. and Coward, A.: Eddy mass transport for the Southern Ocean in an eddy-permitting global ocean model, Ocean Model., 5, 249–266, 2003.

Letcher, T. M.: Climate Change: Observed Impacts on Planet Earth, 1st Edn., Elsevier, 2009.

Lippold, J., Luo, Y., Francois, R., Allen, S. E., Gherardi, J., Pichat, S., Hickey, B., and Schulz, H.: Strength and geometry of the glacial Atlantic Meridional Overturning Circulation, Nat. Geosci., 5, 813–816, doi:10.1038/ngeo1608, 2012.

Lund, D. C., Adkins, J. F., and Ferrari, R.: Abyssal Atlantic circulation during the Last Glacial Maximum: Constraining the ratio between transport and vertical mixing, Paleoceanography, 26, PA1213, doi:10.1029/2010PA001938, 2011.

Lynch-Stieglitz, J., Curry, W. B., and Slowey, N.: Weaker Gulf Stream in the Florida straits during the last glacial maximum, Nature, 402, 644–648, doi:10.1038/45204, 1999.

Lynch-Stieglitz, J., Adkins, J. F., Curry, W. B., Dokken, T., Hall, I., Herguera, J. C., Hirschi, J., Ivanova, E., Kissel, C., Marchal, O., Marchitto, T. M., McCave, I. N., McManus, J. F., Mulitza, S., Ninnemann, U., Peeters, F., Yu, E. F., and Zahn, R.: Atlantic meridional overturning circulation during the Last Glacial Maximum, Science, 316, 66–69, doi:10.1126/science.1137127, 2007.

McDougall, T.: Neutral surfaces in the ocean: implications for modelling, Geophys. Res. Lett., 14, 797–800, 1987.

Madec, G.: NEMO ocean engine, Technical Report 27, Institut Pierre-Simon Laplace (IPSL), 2008.

Manabe, S. and Stouffer, R. J.: Multiple-Century response of a Coupled Ocean-Atmosphere Model to an Increase of Atmospheric Carbon Dioxide, Science, 7, 5–23, doi:10.1175/1520-0442(1994)007<0005:MCROAC>2.0.CO;2, 1994.

Marchitto, T. M. and Broecker, W. S.: Deep water mass geometry in the glacial Atlantic Ocean: A review of constraints from the paleonutrient proxy Cd/Ca, Geochem. Geophy. Geosys., 7, Q12003, doi:10.1029/2006GC001323, 2006.

Martin, P. A., Lea, D. W., Rosenthal, Y., Shackleton, N. J., Sarnthein, M., and Papenfuss, T.: Quaternary deep sea temperature histories derived from benthic foraminiferal Mg/Ca, Earth Planet. Sc. Lett., 198, 193–209, doi:10.1016/S0012-821X(02)00472-7, 2002.

Otto-Bliesner, B. L., Hewitt, C. D., Marchitto, T. M., Brady, E. C., Abe-Ouchi, A., Crucifix, M., Murakami, S., and Weber, S. L.: Last Glacial Maximum ocean thermohaline circulation: PMIP2 model intercomparisons and data constraints, Geophys. Res. Lett., 34 1–6, doi:10.1029/2007GL029475, 2007.

Rahmstorf, S.: Ocean circulation and climate during the past 120,000 years: Nature, 419, 207–14, doi:10.1038/nature01090, 2002.

Schmittner, A., Latif, M., and Schneider, B.: Model projections of the North Atlantic thermohaline circulation for the 21st century assessed by observations, Geophys. Res. Lett., 32, L23710, doi:10.1029/2005GL024368, 2005.

Shin, S., Liu, Z., Otto-Bliesner, B. L., Kutzbach, J. E., and Vavrus, S. J.: Southern Ocean sea-ice control of the glacial North Atlantic thermohaline circulation, Geophys. Res. Lett., 30, 1096, doi:10.1029/2002GL015513, 2003.

Storkey, D., Blockley, E. W., Furner, R., Guiavarc'h, C., Lea, D., Martin, M. J., Barciela, R. M., Hines, A., Hyder, P., and Siddorn, J. R.: Forecasting the ocean state using NEMO: The new FOAM system, Journal of Operational Oceanography, 3, 3–15, 2010

Tagliabue, A., Bopp, L., Roche, D. M., Bouttes, N., Dutay, J.-C., Alkama, R., Kageyama, M., Michel, E., and Paillard, D.: Quantifying the roles of ocean circulation and biogeochemistry in governing ocean carbon-13 and atmospheric carbon dioxide at the last glacial maximum, Clim. Past, 5, 695–706, doi:10.5194/cp-5-695-2009, 2009.

Treguier, A. M., England, M. H., Rintoul, S. R., Madec, G., Le Sommer, J., and Molines, J.-M.: Southern Ocean overturning across streamlines in an eddying simulation of the Antarctic Circumpolar Current, Ocean Sci., 3, 491–507, doi:10.5194/os-3-491-2007, 2007.

Viebahn, J. and Eden, C.: Standing eddies in the meridional overturning circulation, J. Phys. Oceanogr., 42, 1486–1508, doi:10.1175/JPO-D-11-087.1, 2012.

Voldoire, A., Sanchez-Gomez, E., Salas y Mélia, D., Decharme, B., Cassou, C., Sénési, S., Valcke, S., Beau, I., Alias, A., Chevallier, M., Déqué, M., Deshayes, J., Douville, H., Fernandez, E., Madec, G., Maisonnave, E., Moine, M.-P., Planton, S., Saint-Martin, D., Szopa, S., Tyteca, S., Alkama, R., Belamari, S.,

Braun, A., Coquart, L., and Chauvin, F.: The CNRM-CM5.1 global climate model: description and basic evaluation, Clim. Dynam., 40, 2091–2121, doi:10.1007/s00382-011-1259-y, 2012.

Weber, S. L., Drijfhout, S. S., Abe-Ouchi, A., Crucifix, M., Eby, M., Ganopolski, A., Murakami, S., Otto-Bliesner, B., and Peltier, W. R.: The modern and glacial overturning circulation in the Atlantic ocean in PMIP coupled model simulations, Clim. Past, 3, 51–64, doi:10.5194/cp-3-51-2007, 2007.

Wunsch, C.: What is the thermohaline circulation?, Science, 298, 1179–81, doi:10.1126/science.1079329, 2002.

Yu, E. F., Francois, R., and Bacon, M. P.: Similar rates of modern and last-glacial ocean thermohaline circulation inferred from radiochemical data, Nature, 379, 689–694, doi:10.1038/379689a0, 1996.

Zickfeld, K., Eby, M., and Weaver, A. J.: Carbon-cycle feedbacks of changes in the Atlantic meridional overturning circulation under future atmospheric CO_2, Global Biogeochem. Cy., 22, 1–14, doi:10.1029/2007GB003118, 2008.

Zika, J. D., England, M. H., and Sijp, W. P.: The Ocean Circulation in Thermohaline Coordinates, J. Phys. Oceanogr., 42, 708–724, doi:10.1175/JPO-D-11-0139.1, 2012.

Zhang, R., Delworth, T. L., and Held, I. M.: Can the Atlantic Ocean drive the observed multidecadal variability in Northern Hemisphere mean temperature?, Geophys. Res. Lett., 34, L02709, doi:10.1029/2006GL028683, 2007.

Zhang, X., Lohmann, G., Knorr, G., and Xu, X.: Different ocean states and transient characteristics in Last Glacial Maximum simulations and implications for deglaciation, Clim. Past, 9, 2319–2333, doi:10.5194/cp-9-2319-2013, 2013.